Natural gas potential of Carboniferous and Permian transitional shales in central Hunan, South China

Zhao, Zhenghui; Tan, Jianqiang ; Ju, Yiwen; Hilton, Jason; Yang, Rongfeng; Zhou, Ping; Huang, Yanran; Ning, Bowen; Liu, Jisong

[Link to publication on Research at Birmingham portal](#)

Accepted Manuscript

Natural gas potential of Carboniferous and Permian transitional shales in central Hunan, South China

Zhenghui Xiao, Jingqiang Tan, Yiwen Ju, Jason Hilton, Rongfeng Yang, Ping Zhou, Yanran Huang, Bowen Ning, Jisong Liu
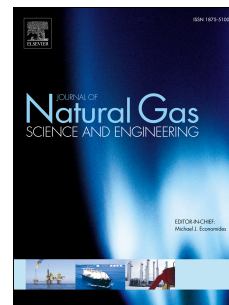
Please cite this article as: Xiao, Z., Tan, J., Ju, Y., Hilton, J., Yang, R., Zhou, P., Huang, Y., Ning, B., Liu, J., Natural gas potential of Carboniferous and Permian transitional shales in central Hunan, South China, *Journal of Natural Gas Science & Engineering* (2018), doi: 10.1016/j.jngse.2018.05.024.

1 **Natural gas potential of Carboniferous and Permian transitional**

2 **shales in central Hunan, South China**

3 Zhenghui Xiao[a], Jingqiang Tan[b,*], Yiwen Ju[c], Jason Hilton[d], Rongfeng Yang[a], Ping Zhou[e],

4 Yanran Huang[a], Bowen Ning[f], Jisong Liu[a]

5

6 [a] Hunan Key Laboratory of Shale Gas Resource Utilization, School of Resource, Environment and Safety

7 Engineering, Hunan University of Science and Technology, Xiangtan 411201, Hunan, China

8 [b] Key Laboratory of Metallogenic Prediction of Nonferrous Metals and Geological Environment Monitoring,

9 Ministry of Education, School of Geosciences and Info-Physics, Central South University, Changsha 410083,

10 China

11 [c] College of Earth Sciences, University of Chinese Academy of Sciences, Beijing 100049, China

12 [d] School of Geography, Earth and Environmental Science, University of Birmingham, Edgbaston, Birmingham,

13 B15 2TT, UK

14 [e] School of Economics, Hunan Institute of Engineering, Xiangtan 411104, Hunan, China

15 [f] Henan Geological Exploration Institute of China Chemical Geology and Mine Bureau, Zhengzhou 450011,

16 Henan, China

17 [*] Corresponding authors: tanjingqiang@aliyun.com

18

19 **Abstract**

20 The Carboniferous Ceshui formation and Permian Longtan and Dalong formations

21 were deposited in transitional settings preserved in what is now central Hunan Province,

22 South China, as they are potential natural gas plays. In this study, we analysed the total

23 organic carbon (TOC), vitrinite reflectance (Ro), kerogen type, mineralogy, porosity,

24 permeability, and methane adsorption of representative shale samples from these rock units.

25 Our results indicate that TOC content can be as high as 9.2%, with a mean ($\bar{x}$) of 3.5%. The

26 Permian shale formations were deposited in more strongly reducing environments than the

27 Carboniferous Ceshui shale. The kerogen composition of the Carboniferous Ceshui shale is

28 dominated by Type III, while both of the Permian shales contain primarily Type II kerogens;

29 Ro values range from 1.1% to 2.4% ($\bar{x}$=1.6%). The organic matter in all the studied shales is

30 in the wet gas window of thermal maturity and is relatively less mature than Lower

31 Palaeozoic marine shales in south China. Mineral compositions are dominated by quartz

32 ($\bar{x}$=53.8%) and clay ($\bar{x}$=35.6%), suggesting a high brittleness index. Porosity ranges from

33 0.5% to 14% ($\bar{x}$=6.4%), while permeability varies from 0.0026 micro Darcy (mD) to 0.0640

34 mD ($\bar{x}$=0.0130 mD). The gas adsorption capacity varies from 1.24 to 4.53 cm^3/g ($\bar{x}$=2.40

35 cm^3/g). Relatively less mature shale samples (Ro<1.5%) have low methane adsorption

36 capacities, regardless of their TOC values. However, the methane adsorption capacity of

37 more mature (Ro>1.5%) shales samples exhibit a positive correlation with TOC content.

38 **Keywords:** Lower Carboniferous; Upper Permian; Natural gas; Transitional shale;

39 Unconventional reservoir; Hunan Province.

40

41 **1. Introduction**

42   The remarkable success of shale gas development in North America has triggered a

43 flourishing of shale gas exploration and increased the number of investigations into the gas

44 potential of shales worldwide (e.g., Bowker, 2007; Jarvie et al., 2007; Tang et al., 2014; Tan

45 et al., 2015). To enhance domestic energy supply via shale gas exploitation, the Chinese

46 government has already set ambitious plans. Geological surveys and exploration activities are

47 underway across the country (Tan et al., 2013). To date, China has begun developing several

48 shale gas fields in the Sichuan Basin (e.g., the Fuling, Weiyuan, and Changning shale gas

49 blocks).

50   In China, three types of organic rich shale are widely distributed in sedimentary

51 basins, comprising marine shales, marine-lacustrine transitional shales (hereafter referred to

2

52   as "transitional shales"), and lacustrine shales (Bu et al., 2015; Tan et al., 2015). Marine

53   shales in the Cambrian and Silurian starta and transitional shales in the Carboniferous and

54   Permian strata are widely distributed cross South China (e.g. Tan et al., 2015; Zou et al.,

55   2010). Although natural gas has been successfully produced from the marine shales,

56   transitional shales have not been yet successfully developed (Dong et al., 2016). In the central

57   part of Hunan, Carboniferous and Permian transitional shales occur in thick and laterally

58   extensive beds (Bao et al., 2016; Gu et al., 2015; Jing et al., 2013; Xu et al., 2015). Previous

59   studies have shown that Carboniferous and Permian paralic coal-bearing strata constitute

60   source rocks for conventional petroleum fields in this region (Wang et al., 2010; Zhan et al.,

61   2006; Zhou et., 2014; Zhu et al., 2012). These transitional shales have been more recently

62   identified as promising targets of shale gas exploration (Bao et al., 2016; Gu et al., 2015;

63   Liang et al., 2014; Luo et al., 2012). National petroleum companies, including Sinopec, have

64   already shown strong interest in developing natural gas resources from transitional shale

65   intervals. Therefore, there is an urgent need to characterise these shale intervals and evaluate

66   their reservoir potential.

67   It has been recognized that no two shale gas systems are exactly alike, and thus

68   exploitation strategies differ from one system to the next (Tan, et al., 2015). However,

69   prolific shale plays are commonly distinguished using certain minimal technical thresholds.

70   These include, but are not limited to: shale lateral extent and effective thickness, organic

71   matter richness, thermal maturity, mineralogy, porosity, permeability, adsorptive capacity,

72   and gas-in-place (GIP) (Bowker, 2007; Jarvie et al., 2007; Tan, et al., 2013; 2015). These

73   indices have been widely applied to evaluate the reservoir potential of marine shales in South

74   China. However, for transitional shales, numerous issues remain concerning the composition

75   and source(s) of organic material, depositional environment, thermal maturity, petrophysical

76   properties, and methane adsorption capacity. Additionally, the correlations among organic

77 materials, mineralogy, and depositional conditions, as well as the influences of porosity and

78 permeability, and the relative effects of total organic carbon (TOC) and thermal maturity on

79 methane adsorption have not been clarified. This study aims to investigate these problems

80 through a systematic characterization of transitional shales from the Carboniferous Ceshui

81 formation and the Permian Longtan and Dalong formations in the central region of Hunan.

82 We comprehensively analysed the TOC content, organic matter type, thermal maturity,

83 mineral composition, reservoir physical properties, and gas adsorption capacity of the shales.

84 We then compared our results with those reported for prolific shale plays in China and the

85 United States. Lastly, we discuss the correlations among the selected reservoir

86 characterisation parameters.

87

88 **2. Materials and Methods**

89 *2.1 Geological setting and shale deposition in central Hunan*

90 The study area is located in the Middle Yangtze Region and in the north of the South

91 China fold system (Fig. 1a). It lies east of the Hengshan Uplift, and west of the Xuefeng

92 Uplift. This region is tectonically composed of five subunits. From north to south they are the

93 Lianyuan Depression, Longshan Uplift, Shaoyang Depression, Guandimiao Uplift, and the

94 Lingling Depression (Fig. 1b). Regional faults extend primarily in the NE-NNE direction,

95 and include the Chengbu-Xinhua fault, Qiyang Arc fault, Miluo-Shaoyang fault, Xinshao-

96 Xinning fault, and Zhuzhou-Shuangpai fault (Fig. 2). Additionally, thrust nappe and gravity

97 gliding structures have been formed by multiple tectonic events. The Lianyuan and Shaoyang

98 depression began forming during the Ordovician at the onset of the Caledonian orogeny. The

99 Qiyang arc was dominantly formed through structural deformation caused by the Triassic

100 Indosinian orogeny (Li, et al., 2013; Wang et al., 2010).

4

101   Shales are well developed in certain formations of the study area. Sedimentary strata

102   are characterized by carbonates interbedded with clastics deposited in the Late Palaeozoic to

103   Middle Triassic. The region has experienced four primary sedimentary cycles from the

104   Devonian to the Permian (Jing et al., 2013; Xu et al., 2015). The first sedimentary cycle

105   occurred between the Tiaomajian and Qiziqiao periods during the Devonian when a

106   transgression initiated during a large-scale geological extension and was followed by a

107   regression generated by the Liujiang orogeny. This cycle resulted in the deposition of the

108   Shetianqiao and Qiziqiao marine shales. The second transgression started in the Mississippian

109   (early Carboniferous), but ended as a full-scale regression in the mid-Mississippian with the

110   deposition   of   the   Ceshui   formation   as   transitional   beds   formed   under   the

111   alternating influences of shallow marine and shoreline environments (Fig. 1c) (Shao et al.,

112   1992). The third cycle was primarily controlled by the Dongwu tectonic movement and is the

113   largest transgression that occurred during the development of the mid- to late Carboniferous

114   paraplatform. However, this transgression was terminated by a full-scale regression during

115   the early Lopingian (late Permian) (Fig. 1c), and coastal marsh shales were subsequently

116   deposited (Gu et al., 2015; Ji et al., 2011). The fourth cycle persisted for a shorter time (i.e.,

117   only during the Lopingian), and resulted in the deposition of the Dalong formation (Fig. 1c).

118   During this time, siliciclastic rocks, siliceous limestone, and shales were deposited in littoral-

119   bathyal-abyssal facies (Fig. 1c) (Feng et al., 1993).

120   *2.2 Samples*

121   Fresh transitional shale samples are exposed in some outcrops of the study area. A

122   total of 96 representative samples were collected from the Shimingqiao (SMQ), Qixingjie

123   (QXJ), Duanpoqiao (DPQ), Tantou (TT), Doulishan (DLS), Nantang (NT), Jilong (JL),

124   Jingzhushan (JZS), Zhaoyang (ZY), Liangshuijing (LSJ), Xiandong (XD), Lumaojiang

5

125 (LMJ), and Douling (DL) sections (Fig. 1b). Generally, shale samples were collected from at

126 least 1 m deep, and every 10 m from the bottom to top of the exposed sections.

2.3 Methods

128 The selected samples were analysed for TOC, vitrinite reflectance (Ro), kerogen type,

129 mineralogy, porosity, permeability, and methane adsorption.

130 TOC contents were measured using a Leco carbon-sulphur analyser and reported as

131 the weight percentage (wt%) of the total rock material. Samples were crushed into a powder

132 <200 mesh, and 1-2 g samples were pyrolysed to 600°C. Thin-sections of 42 samples were

133 prepared for investigation mineral components and structural fabrics. The samples were

134 examined using a Zeiss Axiophot Electronic Microscope equipped with a Carl Zeiss Axiocam

135 digital camera and Axiovision 2.0 software. This system was capable of taking high-

136 resolution photomicrographs under magnification of 10x, 20x, 30x, 40x, and 50x. Kerogen

137 type was analysed by transmitted light microscopy. Thermal maturity, represented by Ro,

138 was determined using a MVP-3 microscope photomultiplier.

139 A total of 25 samples were analysed with a D/max-2600 X-ray diffractometer (XRD)

140 to quantify the principal mineralogical constituents. The diffraction data were recorded from

141 $4°$ to $75°$ 2θ with a step width of $0.02°$, and a counting time of 4 s per step. Experimental

142 conditions were set to 40 kV and 30 mA. The measured data were analysed qualitatively

143 using EVA (Bruker) software, and quantitatively using AutoQuant software.

144 High-resolution scanning electron microscopy (SEM) analysis was performed on

145 representative samples with different TOC contents and lithological types. Small subsamples

146 0.3-0.5 cm thick, 0.5-1.0 cm wide, and >2 cm long were cut and prepared. The subsamples

147 were dried in an oven at 40°C for 24 h to remove moisture. Analysis was conducted using a

148 TESCAN VEGA scanning probe microscope, and images were obtained under high vacuum

149 at 20 kV acceleration voltage.

6

150   Porosity was measured with an ULTRAPORE-200A helium porosimetre.

151   Permeability was tested using an ULTRA-PERMTM200 permeametre. Measurements were

152   performed at room temperature and normal pressure (~23°C, 102 kPa) and 50% humidity.

153   Methane adsorption isotherms were measured for selected moisture-equilibrated

154   samples at 40°C. The experimental procedure was: 1) de-gas the sample, 2) conduct leak

155   tests, 3) determine the void volume as well as the sample volume using helium expansion, 4)

156   evacuate for 60 min at 1 MPa to remove helium, and 5) perform the methane adsorption

157   measurement (Tan, et al., 2014a). The Langmuir isotherm was applied to model gas

158   adsorption capacity. The equation used is: $V=V_L P/(P_L+P)$ (Pan, et al., 2015, and references

159   therein), where V is the volume of absorbed gas, V_L is the Langmuir volume (on the basis of

160   monolayer adsorption), which is the maximum adsorption capacity of the absorbent, P is the

161   gas pressure, and P_L is the Langmuir pressure, at which the absorbed gas content (V) is equal

162   to half of the Langmuir volume (i.e., 0.5 V_L).

163

164   **3. Results**

165   *3.1 Organic geochemical characterization*

166   The TOC content of the 96 shale samples ranges from 0.4% to 9.2% (Table 1), with a

167   mean value of 3.5%. Most of sections exhibit mean TOC contents >2%, indicating that these

168   Carboniferous-Permian transitional shales are typically organic-rich. As shown in Tables 1

169   and 2, the TOC content of samples from different sections varies significantly. In general, the

170   TOC content decreases from the Longtan shale to the Dalong shale, and again in the Ceshui

171   shale.

172   Organics of the shales from the Carboniferous Ceshui formation are principally

173   composed of vitrinite (i.e., euvitrinite and vitrodetrinite). This suggests that the organic

174   matter is more derived from higher plants, and the organic matter constituents are

7

175 characteristic of type III kerogen (Definition can be seen in Appendix 1). In contrast, the

176 kerogen type of the shales from the Permian Longtan and Dalong formations are dominated

177 by exinite (i.e., abundant humic amorphous bodies and a small number of sporopollen bodies).

178 The vitrinite (i.e. euvitrinite and vitrodetrinite) content is less than 30%. This implies that the

179 organics of the Upper Permian shales are primarily type II kerogen (Definition can be seen in

180 Appendix 2).

181   Ro values range from 1.1% to 2.4% ($\bar{x}$=1.6%) (Tables 1 and 2). This suggests that the

182 Carboniferous-Permian transitional shales have entered into a stage of high maturation.

183 Organic matter is located in the late wet gas and dry gas window of thermal maturity.

184 Comparatively, Ro values are high in the Ceshui shale, and gradually reduce from these

185 samples to the Longtan shale, and finally the Dalong shale, reflecting a burial depth control

186 on thermal maturity.

187 *3.2 Mineralogy and lithology*

188 3.2.1 Mineralogy

189   The XRD mineralogical data are shown in Table 2. Major constituents are quartz and

190 clay minerals. Minor mineral components include calcite, feldspar, and pyrite. The quartz

191 content ranges between 39.0% and 86.2% ($\bar{x}$=53.8%) and clay minerals range from 11.0% to

192 69.1% ($\bar{x}$=35.6%). Interestingly, the total amount of brittle minerals (i.e., quartz, feldspar,

193 calcite, and dolomite) is >60% (Table 2), indicating that the condition of the shale is likely

194 favourable for the application of hydraulic fracturing.

195   As shown in Fig. 3 and Table 2, mineralogical composition varies among shale

196 intervals. Some of the Permian Dalong shale samples are characterized by higher contents of

197 quartz and calcite and have lower clay mineral contents than average. The pyrite content of

198 most of the samples is generally below the detection level of XRD technology. Nevertheless,

8

199 some of the Longtan shale samples and others from the Dalong formation exhibit much

200 higher pyrite concentrations that can exceed 10%. Additionally, the clay mineral content of

201 the Ceshui shale samples is generally higher than that from the other two shale intervals.

202 3.2.2 Lithology

203   Based on XRD analysis (Table 2) as well as the structural fabrics identified by thin-

204 section examination (Fig. 4), five primary lithological facies can be distinguished for the

205 shale samples investigated: 1) non-laminated shale, 2) carbonaceous shale, 3) calcareous

206 shale, 4) silty shale, and 5) siliceous shale.

207   Non-laminated shale (Figs. 4b and c) is the most common lithofacies type. Quartz and

208 clay minerals are predominant components, while feldspar and pyrite are relatively rare. The

209 TOC content of non-laminated shale is highly variable, ranging from <1% to >6%.

210   Carbonaceous shale (Figs. 4d and e) is less common than non-laminated shale but is

211 the second most abundant lithofacies type except in the Dalong formation. This lithofacies is

212 dark-coloured and has a high TOC content that is generally >6% (Table 2). The sediments are

213 poorly laminated, and the primary constituents are quartz, clay, pyrite, and organic matter.

214   Calcareous shale is one of the more common lithofacies in shales from the Dalong

215 and Ceshui formations, but it is relatively rare in the Longtan formation (Table 2 and Fig. 4a).

216 The sediments of this lithofacies are typically faintly- to well-laminated depending upon the

217 orientation of the interbedded quartz and organic matter (Fig. 4a). The calcite content in

218 calcareous shale samples accounts for about 30-50%, while TOC content is highly variable,

219 and ranges from <1% to >4% (Table 2).

220   The silty shale is greyish black. It is mainly composed of clay minerals, and a small

221 amount of quartz and feldspar. The TOC content is generally <1%.

222   The siliceous shale is dark-coloured and very hard, and primarily occurs in the Dalong

223   formation. Siliceous shale is characterized by a high quartz content (>85%, Table 2), and the

224   TOC content is commonly higher than that of silty and calcareous shales (Table 2).

225   *3.3 Petrophysical properties*

226   3.3.1 Reservoir storage space

227   SEM analysis was performed on the selected samples to characterize pores and

228   fractures. Organic matter pores, interparticle pores (between grains), intraparticle pores

229   (within mineral grains), and microfractures are all present in the samples (Fig. 5). Organic

230   matter pores (Fig. 5a and b) are well-developed in most of the samples, particularly in high

231   TOC shales. Interparticle pores (Fig. 5b, d and f) can be seen around and between crystals of

232   quartz and feldspar or located within the clay crystals. Intraparticle pores (Figs. 5b–d)

233   primarily occur inside pyrite framboids, and in carbonate- and feldspar-rich samples. Strip-

234   like microfractures often can be seen between clay crystal, or between clay laminae and silty

235   laminae (Figs. 5a, d–e).

236   3.3.2 Porosity and Permeability

237   The results of porosity and permeability analyses are listed in Table 3. Porosity ranges

238   from 0.5% to 14.0% ($\bar{x}$=6.4%) and permeability ranges from 0.0026 micro Darcy (mD) to

239   0.0640 mD ($\bar{x}$=0.0130 mD). Shales from the Longtan formation generally have a higher

240   porosity and permeability than samples from the Dalong and Ceshui formations.

241   *3.4 Gas Adsorption Capacity*

242   The high-pressure methane adsorption capacities (i.e., the maximum adsorbed gas

243   amount) for the moisture-equilibrated shale samples vary from 1.24 cm^3/g to 4.53 cm^3/g

244   ($\bar{x}$=2.40 cm^3/g) (Fig. 6), indicating a strong methane adsorptive potential.

245

4. Discussion

4.1 Organic matter in the shale

248   TOC represents the richness of organic matter in source rocks. Promising

249 conventional or unconventional source rocks generally have high TOC concentrations (Jarvie

250 et al., 2007). Previous studies have suggested that high pyrite content in shales represents

251 strongly reducing environmental conditions that are favourable for the enrichment and

252 preservation of organic matter (Liang et al., 2014; Tan et al., 2014b, 2015; Wu et al., 2014).

253 As shown in Table 2, shales with high pyrite contents tend to have high TOC contents as well.

254 Given the relatively high TOC contents of the shale samples studied here, this suggests that

255 the analysed transitional shales were most likely deposited in strongly reducing conditions. In

256 fact, transitional sedimentary environments in the study area were dominated by stable and

257 anoxic conditions through the depositional period of the shales (Dang et al., 2016; Liang et al.,

258 2014; Tang et al., 2016). Because the Longtan shale normally exhibits higher TOC and pyrite

259 contents, this formation may have been deposited in more strongly reducing environments

260 compared to shales from the Dalong and Ceshui formations. However, the higher TOC

261 concentration may also indicate a better and/or stronger organic input. According to the

262 results of kerogen typing, the organic matter of the Ceshui shale is dominated by type III

263 kerogen, whereas >70% of the macerals from the Permian shale are type II organics. This

264 suggests that most of the organics found in the Permian shales are derived from marine

265 plankton (i.e., marine microflora and microfauna). However, it has previously been

266 documented that more derived, terrestrial plants were extensively distributed in and near the

267 littoral swamps in this part of China during both the Mississippian and Lopingian (e.g., Ji et

268 al., 2011; Shao et al., 1992). While this suggests that the organic input from terrestrial plants

269 for both the Carboniferous and Permian shales should generally be similar, the observed

270 organic matter in the Permian shale includes much more marine plankton than the

271 Carboniferous shale.

4.2 Favourable geological conditions for natural gas accumulation in shales

273 4.2.1 Organic geochemistry

274   High TOC content generally suggests that conventional and unconventional

275 petroleum resources are promising for exploration and exploitation (Dang et al., 2016; Jarvie

276 et al., 2007; Tan et al., 2015). TOC values significantly vary among shale reservoirs, but the

277 productive shale gas plays normally exhibit TOC contents >2% (Tan, et al., 2015). Li et al.

278 (2015) reported that the TOC content of the Longtan shale in South China ranges from 0.4%

279 to 14.6%, with a mean of 4.5%. Gu et al. (2015) and Bao et al. (2016) also documented that

280 more than half of analysed Permian shale samples exhibit TOC contents >2%. Compared to

281 productive shale gas plays in the United States, such as the Barnett shale (Dong et al., 2016),

282 and the transitional shales in the Bohai Bay basin and Southern North China basin (Dang et

283 al., 2016; He et al., 2016;), TOC contents of the transitional shales in the study area are even

284 higher. This indicates that the transitional shales in central Hunan have excellent initial

285 potential for petroleum generation.

286   The organic matter type of current exploration targets for shale gas is primarily

287 dominated by type II kerogen (e.g., the Barnett, Marcellus, and Haynesville shale plays in the

288 United States; the shale gas formations in the Western Canadian basin; and the Longmaxi

289 shale in South China) (Dong et al., 2016) (Table 4). Nevertheless, thick, widespread, gas-

290 saturated, fine-grained, organic rich units containing other types of organic matter, which

291 were subjected to extensive biogenic degradation in the thermally immature stage or

292 significant thermal decomposition in the thermally mature or over mature stages, can also

293 serve as excellent exploration targets (Hamblin, 2006; Martini et al., 2003; Tan et al., 2015).

294 The organic matter of the Carboniferous shales in South China have typically been regarded

12

295 as a type III kerogen (Luo, et al., 2012; Zhang et al. 2014) derived from terrestrial plants. In

296 the Mississippian, organic material in paralic shale and coal seams were both derived from

297 terrestrial plants, including Lycopsids and Equisetopsids (Gu et al., 2015; Zhang et al. 2014).

298 However, the coal seams in the Longtan formation are locally distributed across central

299 Hunan, and the shale with high TOC content does not tend to occur within coal seams (Ji et

300 al., 2011). This might be the reason why the organic matter type of the Permian shale differs

301 from that of the Carboniferous shale. Bao et al. (2016) reported that the kerogen $\delta^{13}C$ values

302 in the Longtan and Dalong shales range from -23‰ to -27‰, further confirming that the

303 organic matter is dominated by type II kerogen, with a minor component of type III kerogen.

304 Most shale gas that is currently produced is primarily a thermogenic gas that was

305 formed by the thermal degradation of organic matter (Tan, et al., 2014c). For example, the

306 highly productive Barnett shale gas play normally has a Ro >1%, while the Lower Silurian

307 Longmaxi shale in South China has a Ro generally >2% (Chen et al., 2011; Tan, et al., 2015;

308 Zhang et al., 2015). Although a minor fraction of shale gas might be of biogenic origin in the

309 thermally immature stage (Martini et al., 2003; Martini et al., 2008), such quantities are

310 significantly less than those of thermogenic shale gas (Tan, et al., 2014c). In addition to the

311 current study, other studies have reported that Ro values of the Longtan and Dalong shales

312 range from 1.1% to 2.4%, with a mean value of 1.6% (Bao et al., 2016; Gu et al., 2015).

313 Zhang et al. (2014) have also documented that the Ro values of the Longtan shale range from

314 1.7% to 2.0%, with a mean value of 1.8%. Compared to the lower Cambrian and Lower

315 Silurian marine shales in or adjacent to the Sichuan basin, which generally exhibit an equal

316 Ro value >2.0%, the transitional shales studied here are less thermally mature. Interestingly,

317 as shown in Tables 1 and 2, Ro values of the transitional shales increase gradually in strata

318 that are stratigraphically older, indicating a burial depth control on thermal maturity.

319 4.2.2 Mineralogical composition

320   To produce shale gas economically, horizontal drilling and hydraulic fracturing are

321   the most popular choices for completing shale gas wells. The mineralogical composition of

322   shale plays affects both the reservoir quality and well completion quality. Detailed

323   characterization of the mineral constituents is thus critical to the identification of exploration

324   targets, and essential for determining how the shale reservoir should be completed (Tan, et

325   al., 2014b).

326   Mineral compositions are closely related to rock mechanics, and directly determine

327   the brittleness of the rock. The brittleness of shale rocks reflects the capability to fail under

328   pressure, and for cracks to remain open once the rock fractures (Rickman et al., 2008). Brittle

329   shales thus generally respond well to well completion treatments. However, ductile shales,

330   which might be fractured during hydraulic fracturing, can also be easily healed after

331   stimulation. It has been recognized that quartz-rich and clay-low zones are commonly the

332   most brittle intervals within a shale formation (Johnston, 2004). Hydraulic fracturing

333   strategies used in the more brittle zones are reported to enhance the overall gas production of

334   the well (Boyer et al., 2006). More specifically, Bowker (2002) has suggested that the brittle

335   Barnett shale intervals are generally composed of 45% quartz, 27% illite, 8% carbonate, 7%

336   feldspar, 5% pyrite, and 3% siderite.

337   One of the most common methods to determine the brittleness of a shale play is based

338   on relative mineral compositions. Jarvie et al. (2007) and Rickman et al. (2008) documented

339   the correlations between mineral composition and brittleness of the Barnett shales. They

340   reported that the most brittle Barnett shales have high quartz contents, and low clay mineral

341   contents. Conversely, the least brittle shales are rich in clay minerals, with relatively minor

342   amounts of quartz. The shales with abundant carbonate are moderately brittle. However, from

343   a stimulation perspective, not all quartz responses equally during well completion. The most

344   effective quartz component for enhancing brittleness appears to be the recrystallized biogenic

345 opaline silica. Detrital quartz, on the contrary, appears to be less effective (Jarvie et al.,

346 2007). The Brittleness Index was proposed based upon the relative proportions of quart group

347 minerals (primarily quartz, feldspar, and pyrite), carbonates, and clay minerals, as: Brittleness

348 Index=quartz/(quartz+carbonates+clays) (Jarvie et al., 2007). Selecting zones in a shale

349 interval that are relatively more brittle is of importance for developing fractures that are large

350 enough to connect the largest rock volume to the wellbore during the well completion

351 process. The geometry of fractures created in brittle shales is different from that of ductile

352 shales. The stimulation treatments carried out on brittle shales can create large, complex

353 fracture networks that expose a large amount of shale surface area, and thus enable

354 commercial gas production (Grieser and Bray, 2007).

355 Mineral compositions are also important for fluid selection during well completion.

356 The determination of mineralogy and fluid sensitivity is essential for optimizing completion

357 and stimulation strategies (Britt and Schoeffler, 2009). In most cases, acid is commonly used

358 to dissolve soluble minerals, increase porosity, and improve the fracturing process. Because

359 carbonate minerals can be easily dissolved even in weak acid solutions, the contents of

360 carbonates evidently correlate with the acid solubility of shale samples (Rickman, et al.,

361 2008). If samples have low carbonate concentrations, they generally show low to moderate

362 acid solubility. In that scenario, mixed fluids of weak acids and surfactants are recommended

363 to roughen the fracture surfaces, increase surface areas, and prevent significant generation of

364 fines that could cause plugging of the fractures created, and damage to perforations

365 (Rickman, et al., 2008). On the other hand, clay swelling is a significant problem for the

366 stability of boreholes and created fractures, and finally on the gas recovery from shale

367 reservoirs. If more smectite or illite/smectite mixed layers are present, the swelling potential

368 of the shale might be substantial. In this case, development then requires more protective

369 strategies, and more rigorous evaluation before the initiation of hydraulic fracturing.

370   The average quartz and clay mineral contents of Permian shales in South China are

371   commonly >50%, and <25%, respectively (Zhang et al., 2016). Meanwhile, Carboniferous

372   shales in the same region exhibit quartz and clay mineral contents of ~60.8% and ~23.3%,

373   respectively (Miao et al. 2016). The highly productive lower Palaeozoic marine shales in

374   South China and the transitional shales in Palaeozoic basins in North China generally contain

375   highly brittle mineral contents (> 60% on average), and low clay mineral contents (< 40% on

376   average) (Chen et al., 2011; Ding et al., 2013; Tan et al., 2014b; Tang et al., 2014; Zhang et

377   al., 2015). Our study also indicates mineral compositions in transitional Carboniferous and

378   Permian shales in South China that are dominated by brittle minerals. These findings could

379   provide valuable insights for reservoir evaluation and stimulation treatments in the future.

380   4.2.3 Petrophysics

381   Intercrystallite pores in pyrite framboids commonly exist in shale samples, and

382   contribute to gas storage (Loucks et al., 2009, 2012). For the analysed transitional shale

383   intervals, pyrite was relatively abundant in shales from the Longtan formation, thus

384   intraparticle pores occur more frequently (Fig. 5b). Intraparticle pores occur in shale samples

385   with relatively high carbonate and/or feldspar contents (Figs. 5b–d). This can be ascribed to

386   the partial dissolution of soluble carbonate and feldspar minerals (Heath, et al., 2011; Loucks

387   et al., 2012). Microfractures (Figs. 5e), which can be formed during catagenesis, are well

388   developed in shale samples with high clay mineral contents (i.e., illitisation could result in

389   microfractures in shale with lengths up to tens of micrometres) (Liang et al., 2014).

390   Previous studies have shown that the average porosity and permeability of the

391   Permian shales in the study area are <2% and ~0.007 mD, respectively (Gu et al., 2015; Bao

392   et al., 2016), whereas the porosity of the Carboniferous Ceshui shale ranges from 1% to 6.2

393   %, with a mean value of 3.5% (Miao, et al., 2016). Compared with these results, porosity and

394   permeability values obtained for the shale samples in our investigation are generally higher

16

395   (Table 3). One of the primary reasons might be that some of the shale samples in the current

396   study have higher TOC contents, and well-developed micro-fractures. As our samples were

397   freshly collected, weathering impact on petrophysical properties should be low. However, our

398   findings suggest that these shale intervals are all characterized by low porosity and ultra-low

399   permeability, which may result in an even tighter reservoir than the Barnett shale (Dong, et

400   al., 2016).

401   To analyse the primary drivers of porosity formation, we examined the correlation

402   between porosity and TOC content (Fig. 7a). There is a positive correlation between TOC

403   content and porosity for most of the selected samples. This suggests that organic matter

404   probably dominates the porosity of the shale. This might also be the reason why the porosity

405   of the Longtan shale is comparatively higher than the less organic-rich shales from the

406   Dalong and Ceshui formations (Table 3). Additionally, there is a negative relationship

407   between the porosity and density (Fig. 7b). This phenomenon might be related to organic

408   matter content because the density of shale tends to decrease as TOC contents increase (Fig.

409   7c). However, a few of the selected samples have higher porosity and permeability, even

410   though they have relatively low TOC (e.g., sample LSJ05; Tables 2 and 3). Through SEM

411   analysis, we found that these samples generally have well developed microfractures (e.g.

412   LSJ05; see Fig. 5e). This could suggest that microfractures can be an important contributor to

413   porosity. For the Barnett shale, microfractures provide migration pathways, and reservoir

414   space for the accumulation of shale gas (Liang et al., 2014; Loucks et al., 2012). However, in

415   this study, correlations between porosity and mineral constituents (e.g. quartz and clay

416   minerals) of the shale remain unclear, and this is likely due to the heterogeneity of the shales.

417   In general, shales exhibit significant anisotropic properties from the nanometre scale

418   to the reservoir scale (e.g., organic and inorganic constituents, mineral types, and structures).

419   For low TOC samples, mineral-associated pores should be dominant. Nevertheless, the

17

420 contribution of organic matter host pores becomes significant if TOC content rises and

421 thermal maturity increases to the gas window. According to research performed on the highly

422 mature (dry gas window) Longmaxi shale in South China, most of the pores in that unit are

423 mineral pores when TOC is less than 0.9%. The contribution of mineral pores is similar to

424 that of organic pores when TOC is in the range of 0.9-1.7%, and organic pores are more

425 significant than mineral pores when TOC is higher than 1.7% (Tang et al., 2016). However,

426 the Barnett shale samples that span a maturity range from a later wet gas window to a dry gas

427 window indicate a positive correlation between TOC and porosity for samples with TOC

428 <5.5%, and little or no correlations for samples with TOC >5.5% (Milliken, et al., 2013).

429 Since quartz, carbonates, and clay minerals are the principal mineral constituents of shales,

430 their relative concentrations can significantly influence porosity because clay minerals are

431 porous, while carbonates can be easily dissolved by geofluids (Ross and Bustin, 2009). In

432 some shales, the pyrite content can be greater than 10%, and pyrite framboids are commonly

433 present. In that context, pyrite-associated pores may also be important.

434   Shales are slowly deposited through suspension in calm waters, and this long

435 deposition period can result in strong vertical heterogeneity in both composition and

436 structure. Lamina, thin sand layers, and bioclasts all vary over time in the investigated shale

437 intervals. As revealed by Pan et al. (2015b), in addition to organic and inorganic constituents,

438 the heterogeneous layering structures in different directions in shales strongly impact porosity

439 and permeability, resulting in anisotropic petrophysical properties. However, porosity and

440 permeability measurements are generally performed on small sample pieces or plugs, and the

441 obtained results are very sensitive to experimental conditions. Therefore, accounting for the

442 petrophysical properties of shales at a large scale requires a very large sample size from

443 across the vertical and spatial extents of the unit. Additional studies with larger sample sizes

444 are needed in the future.

445   4.2.4 Methane adsorption capacity

446   Research by Bao et al. (2016) has previously shown that the average methane

447   adsorption capacity of the Permian Longtan and Dalong shales are 2.7 and 3.5 cm^3/g,

448   respectively, exhibiting a relatively strong gas adsorptive potential. Nevertheless, the

449   Carboniferous-Permian shale intervals have lower methane adsorption capacity compared to

450   the lower Cambrian and lower Silurian marine shales in or adjacent to the Sichuan basin,

451   South China (Tan et al., 2014a; Zhang et al., 2015). The gas adsorption capacity of over

452   mature marine shales is positively correlated with TOC content (Chalmers et al., 2008;

453   Gasparik et al., 2014; Han et al., 2013; Tan et al., 2014a; Wu et al., 2014). However, as

454   shown in Fig. 7, the methane adsorption capacity of TOC-rich samples (i.e. DLS02 and

455   DBQ09) is not always significantly higher than that of TOC-poor samples (i.e. NT02) for the

456   high maturity shales of this study. This suggests that other factors may play more important

457   roles in influencing methane adsorption.

458   Shale samples with Ro values less than 1.5% (i.e., samples DLS02 and DBQ09; Fig. 6)

459   have low gas adsorption capacity irrespective of their TOC values. However, when Ro values

460   of the shale samples are greater than 1.5% (i.e., samples NT02 and JZS09; Fig. 6), their gas

461   adsorption capacity is much higher than that of the shale samples with Ro values <1.5%. This

462   suggests that the gas adsorption capacity might be closely associated with thermal maturity

463   for the high maturity shales. Compared with the two samples with Ro values above 1.5% (i.e.,

464   samples DLS02 and DBQ09; Fig. 6), even when there is little difference in thermal maturity,

465   the gas adsorption capacity of the shale increases greatly with higher TOC content. This

466   implies that the organic matter content might be largely responsible for adsorbing gas in the

467   high maturity range.

468   Micropores hosted in organic matter are the primary factor that influences the

469   adsorption capacity of organic-rich rocks (Loucks, et al., 2012; Tan, et al., 2014a; Tan, et al.,

470 2014b; Zhang et al., 2015; Zhong et al., 2016). However, micropores are poorly developed

471 during the low maturity to oil window range (Ro=0.5-1.0%) but increase dramatically as

472 thermal maturity enters the gas window stage (Ro ≥1.5%) (Xiong et al., 2015). Additionally,

473 organic matter type possibly influences the adsorption capacity of shale and coal samples

474 (Gasparik et al., 2014; Tan et al., 2014a;). The transitional shales in the current study contain

475 moderate amounts of type III organic matter, while the lower Cambrian and lower Silurian

476 marine shales in South China lack type III kerogen. The relatively lower adsorption capacity

477 of the analysed transitional shales can be partially ascribed to the different types of organic

478 matter.

479   The Xiangye-1 well in the study area is the first and, presently, the only natural gas

480 exploration well targeted toward the studied transitional shales (Bao et al., 2016; Gu et al.,

481 2015). During drilling, the Dalong formation shale exhibited very low desorption gas content

482 that was attributed to poor preservation conditions, long periods of tectonic alteration, and

483 extensive thermal evolution (Bao et al., 2016; Gu et al., 2015). Based on the above discussion,

484 the low gas content might also result from the low thermal maturity given that shales with Ro

485 <1.5% generally have less gas adsorption capacity. As shown in Tables 1 and 2, the Ro

486 values for most of the Dalong formation shale samples are <1.5%. The intrinsic reason is that

487 micropores might be relatively less developed in a low thermal maturity range. It should be

488 noted that extrapolations from adsorption data obtained in the lab to *in situ* subsurface

489 geological conditions requires a more comprehensive, multi-factor analysis.

490   In addition to the inherent properties of shales (e.g., organic matter content, mineral

491 constituents, thermal maturity, and pore structure), *in situ* geological conditions of shale

492 reservoirs are fraught with uncertainties. For example, gas adsorption measurements are

493 generally performed in isothermal conditions, whereas the geological temperature varies in

494 reservoirs at different depths. The simulated applied pressure is likely much lower than actual

495   reservoir pressures, given that the burial depth of some of the shale gas reservoirs in South

496   China exceeds 5 km. The moisture content also varies markedly with diagenesis and thermal

497   maturation of organic matter. Moreover, gas adsorption measurements are commonly

498   performed on cuttings or powders that show higher pore surface accessibility than the intact

499   shales underground.

500   Nevertheless, experimental adsorption data provide the basis for GIP estimation,

501   particularly for regions where natural gas production has not yet been achieved, and

502   desorption data are very rare (Gasparik, et al., 2014). The uncertainty of GIP estimation

503   resulting from both inherent and exogenic factors can be controlled through adsorption

504   experiments performed on a number of representative samples, and under a variety of lab

505   conditions, and with enhanced knowledge of the *in situ*, underground geological conditions of

506   shale reservoirs (Gasparik, et al., 2014).

507

508   **5. Conclusions**

509   We conducted a variety of analyses on Carboniferous and Permian transitional shale

510   samples from central Hunan to investigate their natural gas potential. Our primary findings

511   are:

512   1. These shale intervals are abundant in organic matter and were deposited in reducing

513   sedimentary environments. The organic matter type of the Ceshui shale is dominated

514   by type III kerogen, while that of the Permian shale is principally type II. The thermal

515   maturities of the shales have entered into the late wet gas and dry gas window stages,

516   respectively.

517   2. Non-laminated and carbonaceous shale are the dominant lithological types, followed

518   then by calcareous shale, silty shale, and siliceous shale. Quartz and clay minerals are

519 the principal constituents. Pyrite is highly concentrated in certain Permian shale

520 samples, and generally coincides with higher TOC contents.

521 3. Four types of pore structures were identified through SEM analysis (i.e., organic

522 matter pores, interparticle pores, intraparticle pores, and microfractures). The mean

523 porosity for all sample is 6.4%, and the mean permeability is 0.013 mD. TOC and

524 well-developed microfractures can greatly affect the porosity and permeability of the

525 shale.

526 4. The gas adsorption capacity of the transitional shales was found to vary from 1.24

527 cm^3/g to 4.53 cm^3/g, with a mean value of 2.40 cm^3/g under the experimental

528 conditions. Meanwhile, shales with high TOC content and Ro >1.5% exhibit high gas

529 adsorption capacity.

530

539

540 **Appendix**

541 1. Type III kerogen is derived from terrestrial plant debris, much of which remains

542 taxonomically identifiable. Additionally, type III kerogens mostly contain condensed

543 polyaromatics and oxygenated functional groups, with minor aliphatic chains (Tissot and

544 Welte, 1984).

545   2. Type II kerogen is typically derived from a mixture of phytoplankton, zooplankton,

546 and microorganisms (bacteria) that have been deposited in a reducing environment. Though

547 type II kerogens may also include terrestrial debris (pollen spores, plant cuticle, etc.), they are

548 most often found in marine sediments characterized by autochthonous organic matter (Tissot

549 and Welte, 1984).

550

References

552 Bao, S.J., Lin, T., Nie, H.K., Ren, S.M., 2016. Preliminary study of the transitional facies

553   shale gas reservoir characteristics: Taking Permian in the Xiangzhong Depression as an

554   example. *Earth Science Frontiers* 23, 44–53.

555 Bowker, K.A., 2007. Barnett Shale gas production, Fort Worth Basin: issues and discussion.

556   *AAPG Bulletin* 91, 523–533.

557 Boyer C, Kieschnick J, Lewis R., 2006. Producing gas from its source. *Oilfield Review*, 18,

558   36-49.

559 Britt, L., Schoeffler, J., 2009. The geomechanics of a shale play: What makes a shale

560   prospective. In SPE Eastern Regional Meeting. *Society of Petroleum Engineers* 125525, 1-

561   9.

562 Bu, H., Ju, Y., Tan, J., Wang, G., & Li, X., 2015. Fractal characteristics of pores in non-

563   marine shales from the Huainan coalfield, eastern China. *Journal of Natural Gas Science*

564   *and Engineering* 241, 66-177.

565 Chalmers, G.R.L., Bustin, R. M., 2008. Lower Cretaceous gas shales in northeastern British

566   Columbia. Part I: Geological controls on methane sorption capacity. *Bulletin of Canadian*

567   *petroleum geology* 56, 1–21.

568   Chen, S.B., Zhu, Y.M., Wang, H.Y., Liu, H.L., Wei, W., Fang, J.H., 2011. Shale gas

569   reservoir characterization: a typical case in the southern Sichuan Basin of China. *Energy*

570   36, 6609–6616.

571   Dang, W., Zhang, J.C., Tang, X., Chen, Q., Han, S.B., Li, Z.M., Du, X.R., Wei, X.L., Zhang,

572   M.Q., Liu, J., Peng, J.L., Huang, Z.L., 2016. Shale gas potential of Lower Permian

573   marine–continental transitional black shales in the Southern North China Basin, central

574   China: Characterization of organic geochemistry. *Journal of Natural Gas Science and*

575   *Engineering* 28, 639–650.

576   Ding, W.L., Zhu, D.W., Cai, J.J., Gong, M.L., Chen, F. Y., 2013. Analysis of the

577   developmental characteristics and major regulating factors of fractures in marine–

578   continental transitional shale–gas reservoirs: A case study of the Carboniferous–Permian

579   strata in the southeastern Ordos Basin, central China. *Marine and Petroleum Geology* 45,

580   121–133.

581   Dong, D.Z., Wang, Y.M., Huang, X.N., Zhang, C.C., Guan, Q.Z., Huang, J.L., Wang, S.F., Li,

582   X.J., 2016. Discussion about geological characteristics, resource evaluation methods and

583   its key parameters of shale gas in China. *Natural Gas Geoscience* 27, 1583–1601.

584   Feng, Z.Z., He, Y.B., Wu, S.H., 1993. Lithofacies paleogeography of Permian Middle and

585   Lower Yangtze region. *Acta Sedimentologica Sinica* 11, 13–24.

586   Gasparik, M., Bertier, P., Gensterblum, Y., Ghanizadeh, A., Krooss, B. M., Littke, R., 2014.

587   Geological controls on the methane storage capacity in organic–rich shales. *International*

588   *Journal of Coal Geology* 123, 34–51.

589   Grieser, W., Bray, J. 2007. Identification of Production Potential in Unconventional

590   Reservoirs. Society of Petroleum Engineers. doi:10.2118/106623-MS

591 Gu, Z.X., Peng, Y.M., He, Y.B., Hu, Z.Q.; Zhai, Y.J., 2015. Geological conditions of

592   Permian sea–land transitional facies shale gas in the Xiangzhong depression. *Geology in*

593   *China* 42, 288–299.

594 Hamblin, A.P., 2006. The "Shale Gas" concept in Canada: A preliminary inventory of

595   possibilities. *Geological Survey of Canada* 5384:108.

596 Han, S.B., Zhang, J.C., Li, Y.X., Horsfield, B., Tang, X., Jiang, W.L., Chen, Q., 2013.

597   Evaluation of lower Cambrian shale in Northern Guizhou Province, South China:

598   implications for shale gas potential. *Energy & Fuels* 27, 2933–2941.

599 He, J.H., Ding, W.L., Zhang, J.C., Li, A., Zhao, W., Dai, P., 2016. Logging identification and

600   characteristic analysis of marine–continental transitional organic–rich shale in the

601   Carboniferous–Permian strata, Bohai Bay Basin. *Marine and Petroleum Geology* 70, 273–

602   293.

603 Heath J.E., Dewers T.A., McPherson B.J., Petrusak R., Chidsey, Jr. T.C., Rinehart A.J.,

604   Mozley, P.S., 2011. Pore networks in continental and marine mudstones: Characteristics

605   and controls on sealing behavior. *Geosphere* 7, 429–454.

606 Jarvie, D.M., Hill, R.J., Ruble, T.E., Pollastro, R.M., 2007. Unconventional shale–gas

607   systems: the Mississippian Barnett Shale of north–central Texas as one model for

608   thermogenic shale–gas assessment. *AAPG Bulletin* 91, 475–499.

609 Ji, C.W., Shao, L.Y., Peng, Z.Q., 2011. Late permian sequence–paleogeography and coal

610   accumulation in Hunan province. *Journal of China University of Mining & Technology* 40,

611   103–110.

612 Ji, W. M., Song, Y., Jiang, Z. X., Wang, X.Z., Bai, Y.Q., Xing, J. Y., 2014. Geological

613   controls and estimation algorithms of lacustrine shale gas adsorption capacity: a case study

614   of the Triassic strata in the southeastern Ordos Basin, China. *International Journal of Coal*

615   *Geology* 134, 61-73.

616 Jing, L., Pan, J.P., Xu, G.S., Ma, R.L., Yuan, H.F., Luo, X.P., Wu, C.R., 2013. Lithofacies

617   paleogeography characteristics of the marine shale series of strata in the Xiangzhong–

618   Xiangdongnan depression, Hunan, China. *Journal of Chengdu University of Technology*

619   39, 215–222.

620 Johnston, D., 2004. Technological advances expand potential pay. *Oil and Gas Journal*, 102,

621   51-59.

622 Li, G.L., Wang, X.H., Bo, D.Y., Luo, P., Jiang, W., 2015. Potentiality exploration of the

623   Upper Permian Longtan formation shale gas in central and southeastern Hunan Province.

624   *Geological Science and Technology Information* 34, 133–138.

625 Li, H.T., Cao, D.Y., Wang, L.J., Guo, A.J., Li, Y.F., Xu, Hao. 2013. Characteristics and

626   evolution of coal-controlled structures on the east slope of the Xuefengshan Domain in

627   central Hunan province. *Geotectonica et Metallogenia* 37,611-621.

628 Liang, C., Jiang, Z.X., Zhang, C.M., Guo, L., Yang, Y.T., Li, J., 2014. The shale

629   characteristics and shale gas exploration prospects of the Lower Silurian Longmaxi shale,

630   Sichuan Basin, South China. *Journal of Natural Gas Science & Engineering* 21, 636–

631   648.

632 Liang, J.J., Ma, R.L., Bu, S.F., Liu, W.J., Yang, C., 2014. Reservoir characteristics of shale in

633   Xiangzhong depression and Xiangdongnan depression of Hunan, China. *Journal of*

634   *Chengdu University of Technology* 41, 45–54.

635 Loucks, R. G., Reed, R. M., Ruppel, S. C., Jarvie, D. M., 2009. Morphology, genesis, and

636   distribution of nanometer-scale pores in siliceous mudstones of the Mississippian Barnett

637   Shale. *Journal of Sedimentary Research* 79, 848–861.

638 Loucks, R.G., Reed, R.M., Ruppel, S.C., Hammes, U., 2012. Spectrum of pore types and

639   networks in mudrocks and a descriptive classification for matrix–related mudrock pores.

640   *AAPG Bulletin* 96, 1071–1098.

641   Luo, X.P., Liu, J., Xu, G.S., Ma, R.L., Xian, Z.Y., Xu, M., 2012. Geochemical characteristics

642   and isothermal adsorption properties of the Devonian–Carboniferous marine mud shale in

643   the Xiangzhong depression, Hunan, China. *Journal of Chengdu University of*

644   *Technology* 39, 206–214.

645   Martini, A. M., Walter, L. M., McIntosh, J. C., 2008. Identification of microbial and

646   thermogenic gas components from Upper Devonian black shale cores, Illinois and

647   Michigan basins. *AAPG Bulletin* 92, 327-339.

648   Martini, A.M., Walter, L.M., Ku, T.C.W., Budai, J.M., McIntosh, J.C., Schoell, M., 2003.

649   Microbial production and modification of gases in sedimentary basins: A geochemical

650   case study from a Devonian shale gas play, Michigan basin. *AAPG Bulletin* 87, 1355–

651   1375.

652   Pan, Z. and Connell, L.D. 2015. Reservoir simulation of free and adsorbed gas production

653   from shale. *Journal of Natural Gas Science and Engineering* 22, 359-370.

654   Pan, Z., Ma, Y., Connell, L. D., Down, D. I., and Camilleri, M. 2015. Measuring anisotropic

655   permeability using a cubic shale sample in a triaxial cell. *Journal of Natural Gas Science*

656   *and Engineering*, 26, 336-344.

657   Rickman, R., Mullen, M. J., Petre, J. E., Grieser, W. V., & Kundert, D. 2008. A practical use

658   of shale petrophysics for stimulation design optimization: All shale plays are not clones of

659   the Barnett Shale. Society of Petroleum Engineers. doi:10.2118/115258-MS

660   Shao, L.Y., Zhang, P.F., Liu, Q.F., Zheng, M.J., 1992. The Lower Carboniferous Ceshui

661   Formation in central Hunan, South China: depositional sequences and episodic coal

662   accumulation. *Geological Review* 38, 52–58.

663   Slatt, R.M., O'Brien, N.R. 2011. Pore types in the Barnett and Woodford gas. *AAPG Bulletin*

664   95, 2017–2030.

665   Tan, J. Q., Weniger, P., Krooss, B., Merkel, A., Horsfield, B., Zhang, J. C., Boreham, C. J.,

666   Graas, G. V., Tocher, B. A., 2014a. Shale gas potential of the major marine shale

667   formations in the Upper Yangtze Platform, South China, Part II: Methane sorption

668   capacity, *Fuel* 129, 204–218.

669   Tan, J.Q., Horsfield, B., Fink, R., Krooss, B., Schulz, H. M., Rybacki, E., Zhang, J.C.,

670   Boreham, C. J., Graas, G.V., Tocher, B.A., 2014b. Shale gas potential of the major marine

671   shale formations in the Upper Yangtze platform, South China, Part III: mineralogical,

672   lithofacial, petrophysical, and rock mechanical properties. *Energy Fuels* 28, 2322–2342.

673   Tan, J.Q., Horsfield, B., Mahlstedt, N., Zhang, J.C., diPrimio, R., Vu, T. A. T., Boreham,

674   C. J., Graas, G. V., Tocher, B. A., 2013. Physical properties of petroleum formed during

675   maturation of Lower Cambrian shale in the upper Yangtze Platform, South China, as

676   inferred from PhaseKinetics modelling. *Marine & Petroleum Geology* 48, 47–56.

677   Tan, J.Q., Horsfield, B., Mahlstedt, N., Zhang, J.C., Boreham, C. J., Hippler, D., Graas, G. V.,

678   Tocher, B. A., 2015. Natural gas potential of Neoproterozoic and lower Palaeozoic marine

679   shales in the Upper Yangtze Platform, South China: geological and organic geochemical

680   characterization. *International Geology Review* 57, 305-326.

681   Tang, S., Zhang, J.C., Elsworth, D., Tang, X., Li, Z. M., Du, X. R., Yang, X.Q., 2016.

682   Lithofacies and pore characterization of the Lower Permian Shanxi and Taiyuan shales in

683   the southern North China Basin. *Journal of Natural Gas Science & Engineering* 36, 644–

684   661.

685   Tang, X., Zhang, J.C., Wang, X.Z., Yu, B.S., Ding, W.L., Xiong, J.Y., Yang, Y.T., Wang,

686   L.,Yang, C., 2014. Shale characteristics in the southeastern Ordos Basin, China:

687   implications for hydrocarbon accumulation conditions and the potential of continental

688   shales. *International Journal of Coal Geology* 128, 32–46.

689   Tissot B P, Welte D H. 1984. Petroleum Formation and Occurrence. Springer-Verlag, 1984.

690 Wang, J., Li, S.Z., Jin, C., Wang, Y.J., Zhang, G.W., Liu, L.P., Liu, X. 2010. Dome-and-

691   basin pattern in central Hunan province: stages and genesis of fold superposition.

692   *Geotectonica et Metallogenia* 34, 159-165.

693 Wang, M.Y., Guo, J.L., Kuang, L.X., Zhu,T., 2010. Geochemical characteristics and

694   evolution of the hydrocarbon source rocks from Lianyuan Depression in the middle of

695   Hunan province. *Natural Gas Geoscience* 21, 721–726.

696 Wu, Y., Fan, T.L., Zhang, J.C., Jiang, S., Li, Y.F., Zhang, J.P., Xie, C., 2014.

697   Characterization of the upper Ordovician and lower Silurian marine shale in northwestern

698   Guizhou province of the upper Yangtze block, South China: Implication for shale gas

699   potential. *Energy Fuels* 28, 3679–3687.

700 Xiong, J.Y., Li, S.T., Tang, X., Chen, R.Y., Wang, M., Huang, Z.L., Sun, X.N., Du, K.F,

701   2015. Organic matter occurrence and microscopic mechanism of pore formation in the

702   lacustrine tight carbonate reservoirs. *Oil & Gas Geology* 36, 756–765.

703 Xu, F.H., Qian, J., Yuan, H.F., Xu, G.S., Liang, J.J., 2015. Sedimentary mode and reservoir

704   properties of mud shale series of strata in Xiangzhong–Xiangdongnan depression, Hunan,

705   China. *Journal of Chengdu University of Technology* 42, 80–89.

706 Xu, Y.G., Qi, K.L., 2005. Reconsideration on marine petroleum exploration prospects in the

707   middle Hunan depression. *Petroleum Geology & Expeximent* 27, 594–596.

708 Zhan, G.J., Liu, G.X., Guan, H.L., Fang, C.M, Deng, M., 2006. Genetic types of natural gas

709   of Xiangzhong depression. *Natural Gas Geoscience* 21, 721–726.

710 Zhang, C.L., Tang, S.H., Fan, E.P., Wang, S.B., Sun, C.H., Sun, J.J., 2014. Shale gas

711   reservoir characteristics of Longtan Formation in Lianyuan Depression. *Journal of Oil &*

712   *Gas Technology* 36, 32–36.

713 Zhang, G, T, Chen, X, H,, Zhang, B. M., Li, H., 2016. Physical property characteristics of

714 Permian shale reservior in the Shaoyang Depression, central Hunan province.

715 *Geology and Mineral Resources of South China* 32, 149–158.

716 Zhang, J.P., Fan, T.L., Li, J., Zhang, J.C., Li, Y.F, Wu, Y., Xiong, W.W., 2015.

717 Characterization of the Lower Cambrian Shale in the Northwestern Guizhou Province,

718 South China: Implications for Shale–Gas Potential. *Energy Fuel* 29, 6383–6393.

719 Zhang, L.T., Guo, J.H., Jiao, P., Zhang, Z., 2014. Accumulation conditions and exploration

720 potential of shale gas of Lower Carboniferous in Lianyuan Depression in the middle of

721 Hunan Province. *Journal of Central South University* 45, 2268–2277.

722 Zhong, J.A., Chen, G.J., Lv, C.F., Yang, W., Xu, Y., Yang, S., Xue, L.H., 2016.

723 Experimental study of the impact on methane adsorption capacity of continental shales

724 with thermal evolution. *Journal of Natural Gas Geoscience* 1, 165–172.

725 Zhou, X.K., Guo, J.H., 2014. Petroleum accumulation characteristics and preservation

726 conditions of Lianyuan sag in the central Hunan. *Journal of Geomechanics* 20, 222–229.

727 Zhu, W., Yi, J.Z., 2012. Analyses on the complex geologic structure and its gas exploration

728 potential in Lianyuan region of middle Hunan province. *Special Oil & Gas Reservoirs* 19,

729 35–38.

730 Zou, C.N., Dong, D.Z., Wang, S.J., Li, J.Z., Li, X.J., Wang, Y.M., Li, D.H., Chen, K.M.,

731 2010. Geological characteristics, formation mechanism and resource potential of shale gas

732 in China. *Petroleum Exploration and Development* 6, 641–653.

733

734 **Fig. 1.** (a) Outline map of China showing position of Hunan Province and study area. (b)

735 Regional geological map of the study area and sampling locations. (c) Generalized

736 stratigraphic column of Carboniferous-Permian strata of the study area with stars marking

737 position of target shales (modified from Jing et al., 2013).

738

739   **Fig**. 2. Structural geology map of central Hunan (Modified from Li et al. 2013)

740

741   **Fig. 3.** Ternary diagram of mineralogical constituents.

742

743   **Fig. 4.** Petrological images of Carboniferous-Permian transitional shale samples from the

744   study area. (a) Calcareous shale (QXJ05) from the Lopingian aged Dalong formation at the

745   Qixingjie section. Quartz and carbonate concentrate in white laminae, while clay and organic

746   matter concentrate in black laminae. (b) Non-laminated shale (DPQ06) from the Lopingian

747   aged Dalong formation at the Duanpoqiao section; dark area is mainly composed of organic

748   matter and clay, while the light area primarily comprises quartz and feldspar. (c) Non-

749   laminated shale (NT02) from the Lopingian aged Longtan at the Nantang section; dark area

750   consists of organic matter and clay, and the light is mainly quartz. (d) Carbonaceous shale

751   (DLS05) from the Lopingian aged Longtan formation at the Doulishan section; dark area is

752   mainly organic matter and clay, and the light is mainly quartz and feldspar. (e) Silty shale

753   (LMJ06) from the Mississippian aged Ceshui formation at the Lumaojiang section; clay

754   minerals occupy a large area in the texture, while organic matter and quartz are scattered

755   amongst the matrix. (f) Carbonaceous shale (LSJ04) from the Mississippian aged Ceshui

756   formation at the Liangshuijing section; dark area is mainly organic matter and light area is

757   mainly quartz. Organic matter aggregates or particles are randomly distributed in the matrix.

758

759   **Fig. 5.** SEM images of Carboniferous–Permian transitional shale samples from the study

760   area. (a) Carbonaceous shale (LSJ04) from the Mississippian aged Ceshui formation at the

761   Liangshuijing section; "honeycomb" organic pores and micro-fractures are well developed.

762   (b) Carbonaceous shale (DLS05) from the Lopingian aged Longtan formation at the

763   Doulishan section; interparticle pores exist between pyrite framboids or between pyrite

764   crystals and clay flakes. Intra–particle pores in the feldspar minerals and "honeycomb"

765   organic–matter pores generated by hydrocarbon expulsion are well developed. (c) Calcareous

766   shale (QXJ02) from the Lopingian aged Dalong formation at the Qixingjie section;

767   intraparticle pores in the carbonate minerals are well developed. (d) Transitional shale

768   (DPQ03) from the Lopingian aged Dalong formation at the Duanpoqiao section; inter–

769   particle pores occur between quartz minerals, intra–particle pores exist in the feldspar

770   minerals and micro-fractures in clay minerals and at weak interfaces are well developed. (e)

771   Carbonaceous shale (LSJ05) from the Mississippian aged Ceshui formation at the

772   Liangshuijing section; micro-fractures between clay flakes or between clay laminae and silty

773   laminae are well developed. (f) Silty shale (LMJ06) from the Mississippian aged Ceshui

774   formation at the Lumaojiang section; micro-fractures between clay flakes are well developed.

775

776   **Fig. 6.** Methane adsorption isotherms at 40 °C

777

778   **Fig. 7.** Correlation plots for Carboniferous-Permian shale samples in Central Hunan Province

779   plotting (a) porosity with TOC content, (b) porosity with density, and (c) TOC content with

780   density.

781

782   **Table 1.** TOC and Ro values from the Carboniferous–Permian transitional shale in central

783   Hunan.

784

785   **Table 2.** Results of TOC, Ro and XRD mineralogy for some representative transitional shale

786   samples from central Hunan.

787

788 **Table 3.** Rock density, porosity, and permeability for Carboniferous–Permian transitional

789 shale in central Hunan.

790

791 **Table 4.** Comparison of the shale gas reservoir rocks in central Hunan with other worldwide

792 shale gas source rocks. Setting = depositional environment of source rocks; TOC – Total

793 Organic Carbon; Kerogen = Kerogen Type; Ro = Vitrinite reflectance values; GAC = Gas

794 adsorbtion capacity. Data for Ceshui, Dalong and Longtan shales from this paper; sources for

795 other data from the study by Dong et al. (2016).

Tables

Table 1. TOC and Ro of Carboniferous–Permian shale in central Hunan

Formation	Sections(code)	TOC (%)			Ro (%)		
		Min value	Max value	Mean value	Min value	Max value	Mean value
Dalong	Shimingqiao(SMQ)	0.4	5.0	3.3	1.1	1.4	1.3
Dalong	Qixingjie(QXJ)	0.6	4.6	2.3	1.2	1.7	1.4
Dalong	Duanpoqiao(DPQ)	0.9	6.6	4.8	1.2	1.8	1.5
Dalong	Tantou(TT)	0.5	4.8	2.2	1.2	1.7	1.5
avg.		0.6	5.3	3.2	1.2	1.7	1.4
Longtan	Qixingjie(QXJ)	0.8	8.8	4.4	1.2	1.9	1.5
Longtan	Doulishan(DLS)	6.9	8.8	7.8	1.4	1.5	1.4
Longtan	Nantang(NT)	2.4	5.3	4.0	1.1	1.6	1.4
Longtan	Jilong(JL)	2.6	9.2	6.0	1.6	1.9	1.7
Longtan	Tantou(TT)	1.8	6.2	3.6	1.1	1.9	1.6
avg.		2.9	7.7	5.2	1.3	1.8	1.5
Ceshui	Jingzhushan(JZS)	0.8	6.1	2.4	1.3	2.8	1.8
Ceshui	Zhaoyang(ZY)	2.2	9.0	4.5	1.6	2.2	1.9
Ceshui	Liangshuijing(LSJ)	0.4	7.4	1.8	1.5	2.4	2.1
Ceshui	Xiandong(XD)	0.4	1.6	1.2	1.4	1.8	1.7
Ceshui	Lumaojiang(LMJ)	0.7	2.0	1.3	1.2	1.9	1.5
Ceshui	Douling(DL)	0.8	3.6	2.4	1.4	2.0	1.8
avg.		0.9	5.0	2.3	1.4	2.2	1.8

Table 2. Results of TOC, Ro and XRD mineralogy for some representative shale samples

ID	Formation	samples	Lithofacies	TOC (%)	Ro (%)	quartz (%)	feldspar (%)	carbonate (%)	pyrite (%)	clay (%)
1	Dalong	QXJ02	Calcareous shale	0.6	1.7	39.1	0.0	35.2	0.0	25.7
2	Dalong	QXJ05	Calcareous shale	4.6	1.2	50.6	0.0	30.0	1.3	18.1
3	Dalong	QXJ08	black siliceous shale	3.2	1.2	86.2	2.8	0.0	0.0	11.0
4	Dalong	DPQ02	Calcareous shale	0.9	2.0	52.6	4.6	32.7	0.0	10.1
5	Dalong	DPQ03	black shale	5.9	1.8	43.8	12.5	1.6	0.0	42.1
6	Dalong	DPQ06	black shale	6.1	1.5	79.3	4.4	0.0	4.3	12
7	Dalong	DQ09	black shale	6.3	1.3	53.8	1.4	0.0	13.1	31.7
8	Longtan	DLS02	black carbonaceous shale	8.8	1.4	47.6	14.2	0.0	13.1	25.1
9	Longtan	DLS05	black carbonaceous shale	6.9	1.5	48.9	4.3	0.0	8.9	37.9
10	Longtan	NT02	black shale	3.2	1.6	64.6	0.0	0.0	0.0	35.4
11	Longtan	NT03	black shale	3.1	1.5	70.3	0.0	0.0	0.0	29.7
12	Longtan	QXJ10	black carbonaceous shale	8.2	1.8	50.8	0.0	0.0	9.2	40.0
13	Longtan	QXJ14	black shale	3.5	1.4	50.0	2.4	0.0	1.0	46.6
14	Ceshui	XD01	dark–grey shale	1.5	1.8	53.7	0.0	0.0	0.0	46.3
15	Ceshui	XD06	dark–grey shale	0.4	1.7	62.9	0.5	1.1	0.0	35.5
16	Ceshui	JZS05	dark–grey shale	1.4	2.4	60.4	0.0	0.0	0.0	39.6
17	Ceshui	JZS07	dark–grey shale	1.3	1.6	54.4	0.0	0.0	0.0	45.6
18	Ceshui	JZS09	black carbonaceous shale	6.1	1.7	29.2	0.0	1.7	0.0	69.1
19	Ceshui	LMJ02	dark–grey shale	1.2	1.6	52.2	0.0	0.0	0.0	47.8
20	Ceshui	LMJ06	silty shale	0.7	1.7	39.0	0.0	0.0	3.7	57.3
21	Ceshui	ZY04	black shale	2.3	2.0	50.9	0.0	0.7	8.6	39.8
22	Ceshui	ZY08	Calcareous shale	2.2	2.1	19.3	0.0	48.2	4.8	27.7
23	Ceshui	LSJ01	black carbonaceous shale	10.7	2.0	63.7	0.0	0.0	0.0	36.3
24	Ceshui	LSJ04	black carbonaceous shale	7.4	2.1	60.0	0.0	0.0	0.0	40.0
25	Ceshui	LSJ05	dark–grey shale	0.4	2.4	61.5	0.0	0.0	0.0	38.5

Table 3. Rock Density, Porosity, and Permeability for Carboniferous–Permian shale in central Hunan

ID	Formation	samples	TOC (%)	Rock density (g/cm^3)	Porosity (%)	Permeability (mD)
1	Dalong	QXJ02	0.6	2.60	0.5	0.0032
2	Dalong	QXJ05	4.6	2.53	5.2	0.0040
4	Dalong	DPQ02	0.9	2.51	4.2	0.0031
5	Dalong	DPQ03	5.9	2.62	5.1	0.0072
6	Dalong	DPQ06	6.1	1.49	12.0	0.0470
7	Dalong	DPQ09	6.3	2.40	6.9	0.0026
8	Longtan	DLS02	8.8	1.66	14.0	0.0067
9	Longtan	DLS05	6.9	1.78	8.2	0.0089
10	Longtan	NT02	3.2	1.45	5.6	0.0034
11	Longtan	NT03	3.1	1.46	9.2	0.0250
15	Ceshui	XD06	0.4	2.60	1.4	0.0045
16	Ceshui	JZS05	1.4	2.57	2.3	0.0034
22	Ceshui	ZY08	2.2	2.53	4.7	0.0046
24	Ceshui	LSJ04	7.4	2.06	8.6	0.0640
25	Ceshui	LSJ05	0.4	2.06	8.0	0.0110

Table 4. Comparison of the shale gas reservoir rocks in central Hunan with other worldwide shale gas source rocks. Setting = depositional environment of source rocks; TOC – Total Organic Carbon; Kerogen = Kerogen Type; Ro = Vitrinite reflectance values; GAC = Gas adsorbtion capacity. Data for Ceshui, Dalong and Longtan shales from this paper; sources for other data from the study by Dong et al.(2016).

Shale unit	Ceshui shale (China)	Dalong Shale (China)	Longtan Shale (China)	Wufeng-Longmaxi Shale(China)	Haynesville Shale (US)	Woodford shale (US)	Barnett Shale (US)
Age	Carboniferous	Permian	Permian	Ordovician-Silurian	Jurassic	Devonian	Carboniferous
Setting	Transitional	Transitional	Transitional	Marine	Marine	Marine	Marine
TOC (%)	0.4–9.0 ($\overline{x}$=2.3)	0.4–6.6 ($\overline{x}$=3.2)	0.8–9.2 ($\overline{x}$=5.2)	0.4–25.7 ($\overline{x}$=2.6)	3.0	5.3	3.7
Kerogen	III	II	II	I – II	I – II$_1$	I – II$_1$	II$_1$
Ro (%)	1.8–2.8 ($\overline{x}$=1.8)	1.1–1.8 ($\overline{x}$=1.4)	1.1–1.9 ($\overline{x}$=1.5)	1.6-3.6	1.5	1.5	1.6
Brittle minerals (%)	30.9–67.5 ($\overline{x}$=55.0)	55.2–89.9 ($\overline{x}$=75.8)	50.8–70.3 ($\overline{x}$=58.9)	21.0-44.0	35.0-65.0	50.0-75.0	40.0-60.0
Porosity (%)	1.4-8.6 ($\overline{x}$=5.0)	0.5-12.0 ($\overline{x}$=5.7)	5.6-14.0 ($\overline{x}$=9.3)	5.2	8.3	5.0	5.0
Permeability (mD)	0.003-0.064 ($\overline{x}$=0.018)	0.003-0.047 ($\overline{x}$=0.011)	0.003-0.025 ($\overline{x}$=0.011)	0.221	0.350	0.050	0.050

Figures

Figure1 (a) The position of Hunan Province and study area; (b) Regional geological map and sampling locations; (c) Generalized stratigraphic column of Permo-Carboniferous strata of the study area (Modified after Jing et al., 2013).
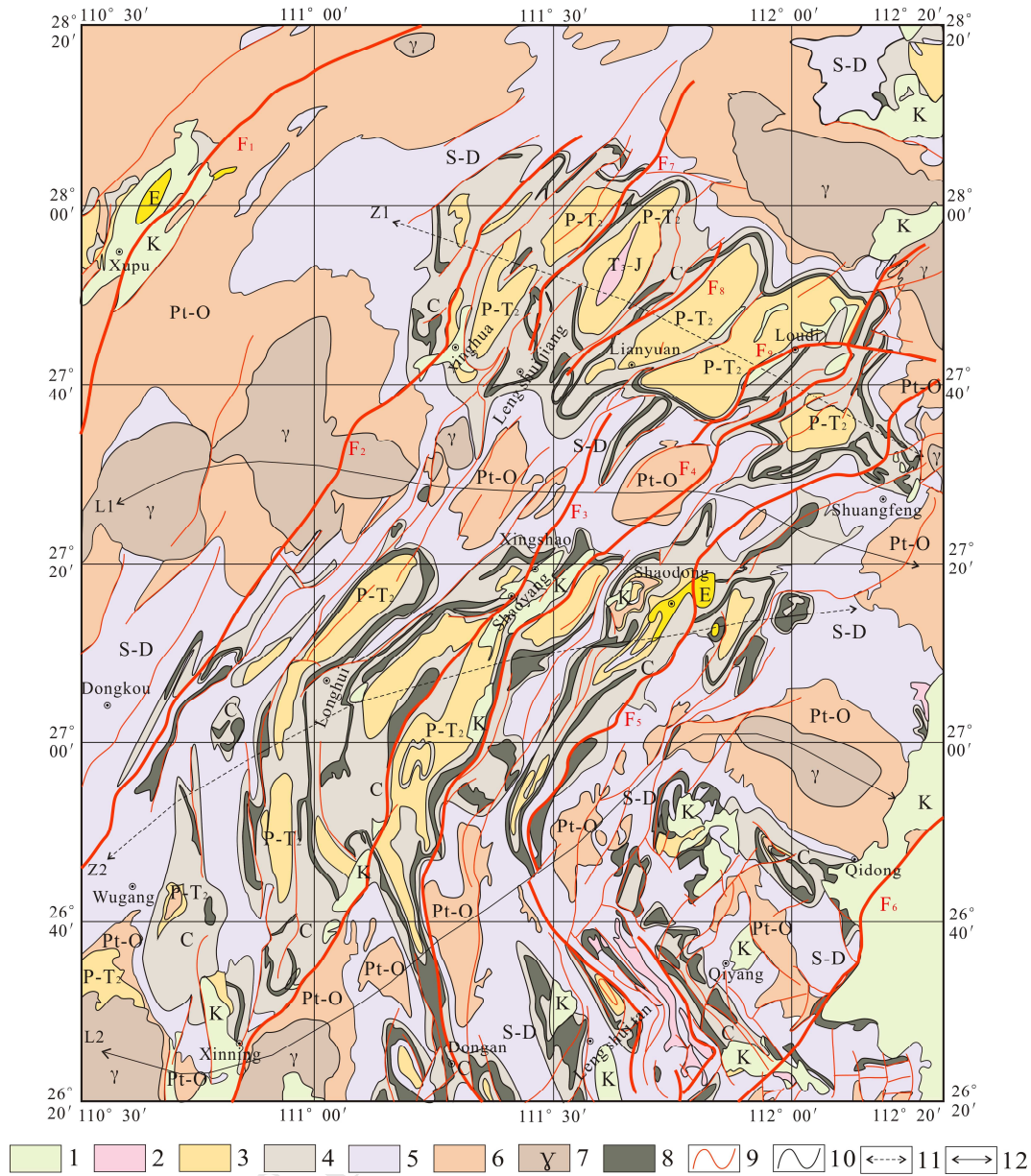
Figure 2 Structure geology map of the central Hunan (Modified from Li et al. 2013). 1. Cretaceous; 2. Upper Triassi-Jurassic; 3. Permian-Middle Triassic; 4. Carboniferous; 5. Silurian-Devonian; 6. Proterozoic-Ordovician; 7. Magmatic body; 8. Coal measures; 9. Fault line; 10. Stratigraphic boundary; 11. Depression; 12. Uplift; F1. Anhua-Xupu fault; F2. Chengbu-Xinhua fault; F3. Xinshao-Xinning fault; F4. Miluo-Shaoyang fault; F5. Qiyang Arc fault; F6. Zhuzhou-Shuangpai fault; F7. Jiyun fault; F8. Jinpanlun fault; F9. Fengguanshan fault; Z1. Lianyuan Depression; Z2. Shaoyang Depression; L1. Baimashan-Longshan bead-shape uplift; L2. Niuxingzhai-guandimiao bead-shape uplift.
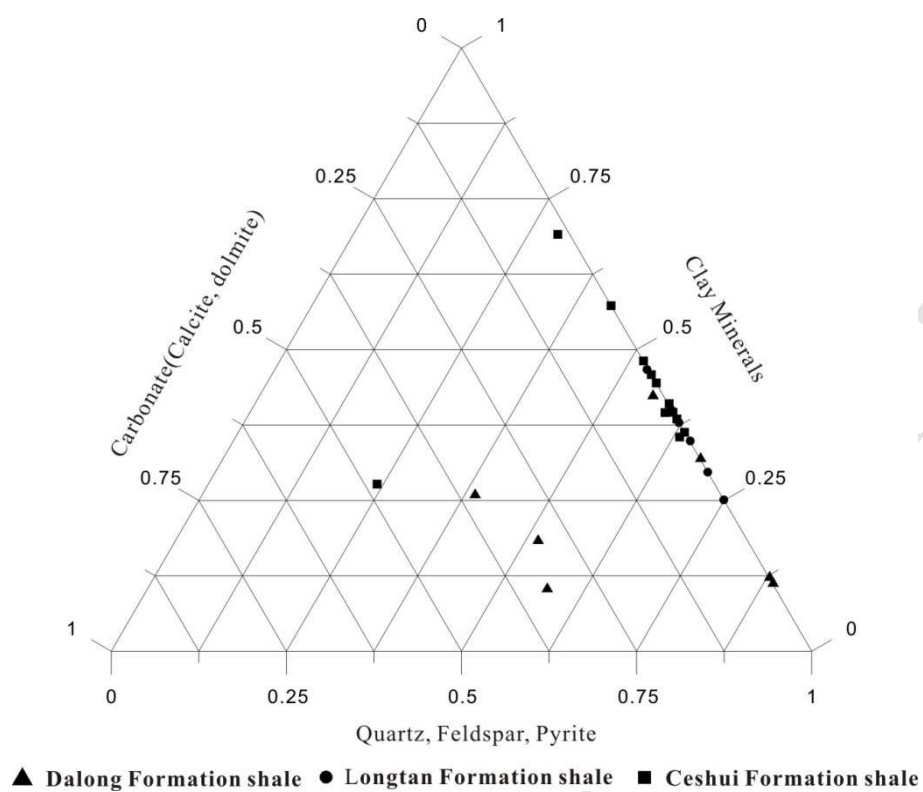
Figure 3. Ternary diagram of mineralogical constituents
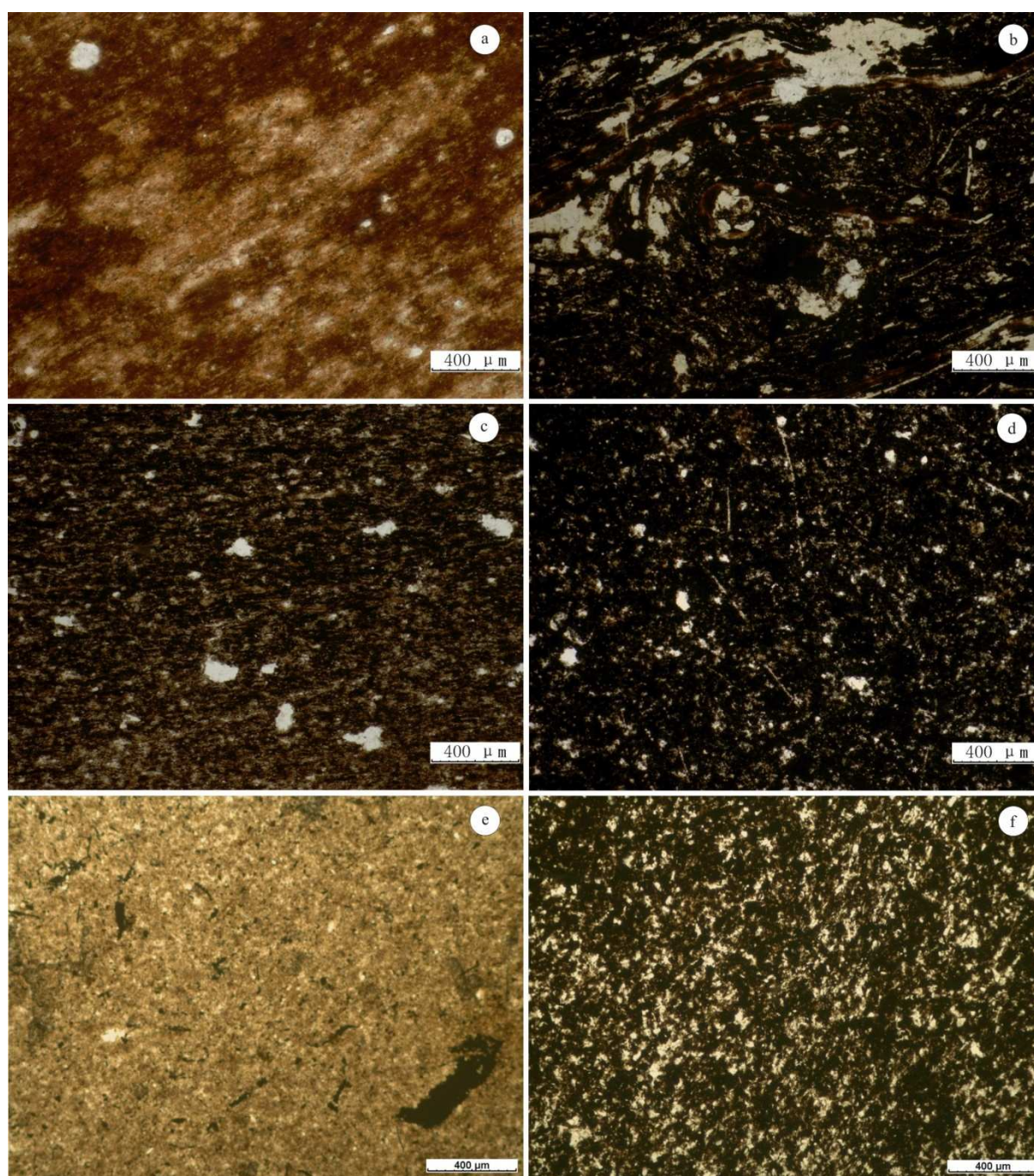
Figure 4. Micro-photographic images of Carboniferous-Permian shale samples. (a) Upper Permian Dalong calcareous shale (QXJ05) from the Qixingjie section. Quartz and carbonate concentrate in the white laminae, while clay and organic matter concentrate in the black laminae. (b) Upper Permian Dalong nonlaminated shale (DPQ06) from the Duanpoqiao section. The dark area is mainly composed of organic matter and clay, while the light area primarily comprises quartz and feldspar. (c) Upper Permian Longtan nonlaminated shale (NT02) from the Nantang section. The dark area consists of organic matter and clay, and the light is mainly quartz. (d) Upper Permian Longtan carbonaceous shale (DLS05) from the Doulishan section. The dark area is mainly organic matter and clay, and the light is mainly quartz and feldspar. (e) Lower Carboniferous Ceshui silty shale (LMJ06) from the

4

Lumaojiang section. Clay minerals occupy a large area in the texture, while organic matter and quartz scatter in the matrix. (f) Lower Carboniferous Ceshui carbonaceous shale (LSJ04) from the Liangshuijing section. The dark place is mainly organic matter and the light is mainly quartz. Organic matter aggregates or particles are randomly distributed in the matrix.
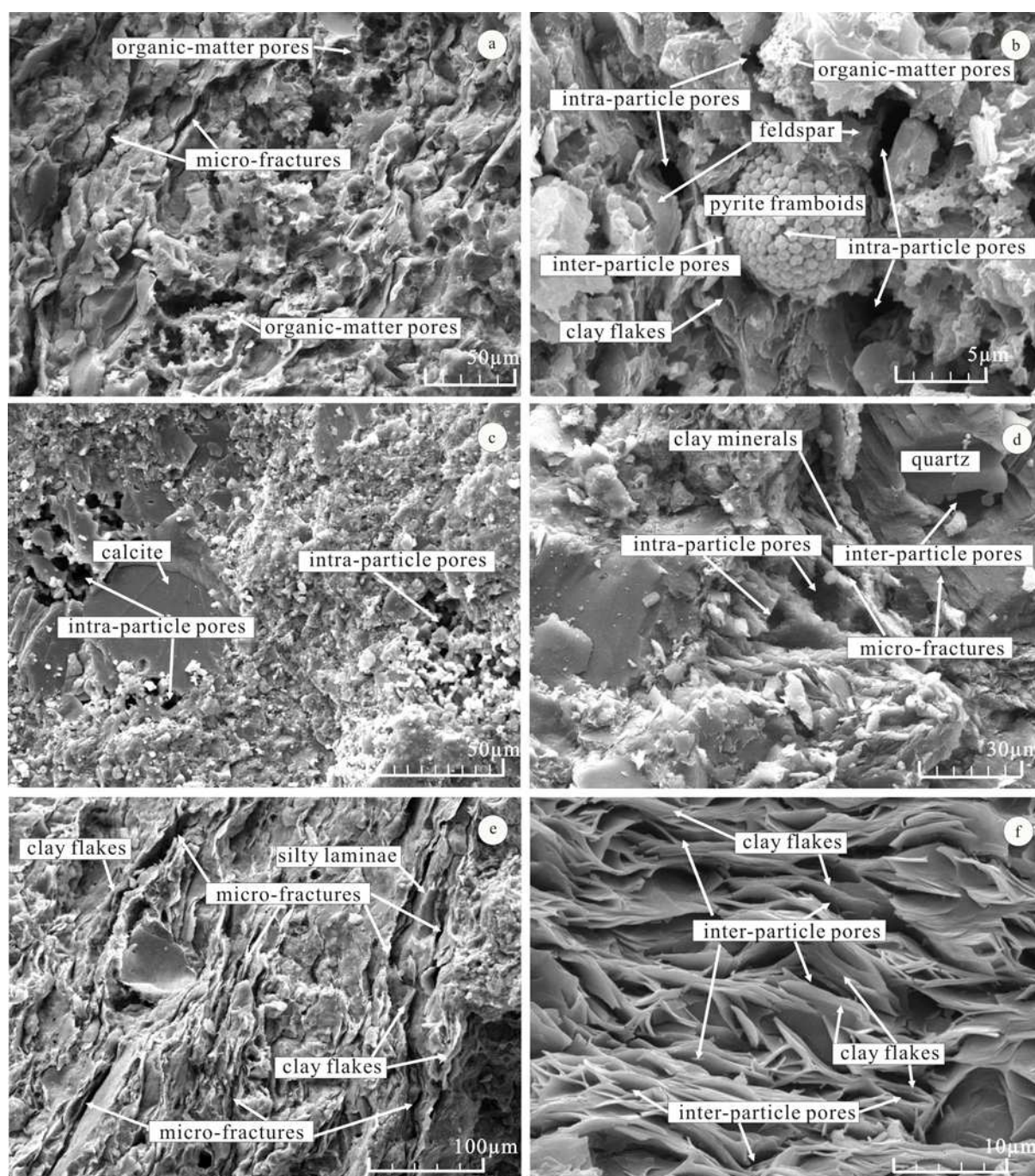
Figure 5. SEM images of Carboniferous–Permian shale samples. (a) Lower Carboniferous Ceshui carbonaceous shale (LSJ04) from the Liangshuijing section. "Honeycomb" organic pores and miro-fractures are well developed. (b) Upper Permian Longtan carbonaceous shale (DLS05) from the Doulishan section. Intra-particle pores exist in the pyrite framboids and the feldspar minerals. Inter–particle pores between pyrite crystals and clay flakes, and "honeycomb" organic–matter pores generated by hydrocarbon expulsion are well developed. (c) Upper Permian Dalong calcareous shale (QXJ02) from the Qixingjie section. Intra-particle pores in the carbonate minerals are well developed. (d) Upper Permian Dalong shale (DPQ03) from the Duanpoqiao section. Inter–particle pores occur between quartz minerals, intra–particle pores exist in the feldspar minerals and miro-fractures in clay

minerals and at weak interfaces are well developed. (e) Lower Carboniferous Ceshui carbonaceous shale (LSJ05) from the Liangshuijing section. Micro-fractures between clay flakes or between clay laminae and silty laminae are well developed. (f) Lower Carboniferous Ceshui silty shale (LMJ06) from the Lumaojiang section. Inter-particle pores in the clay flakes are well developed.
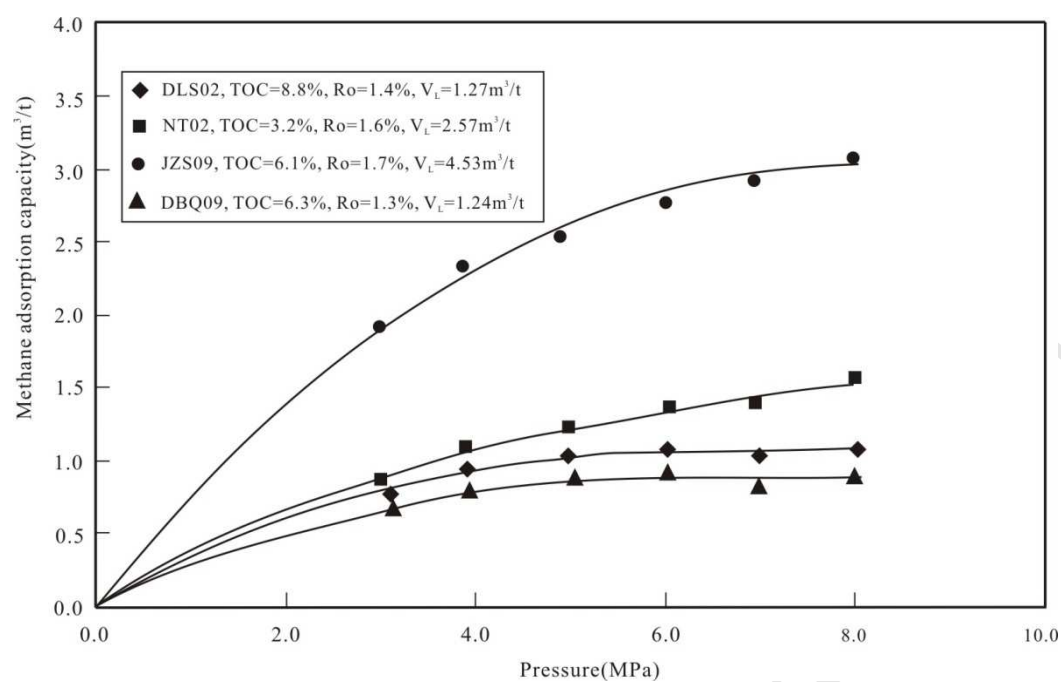
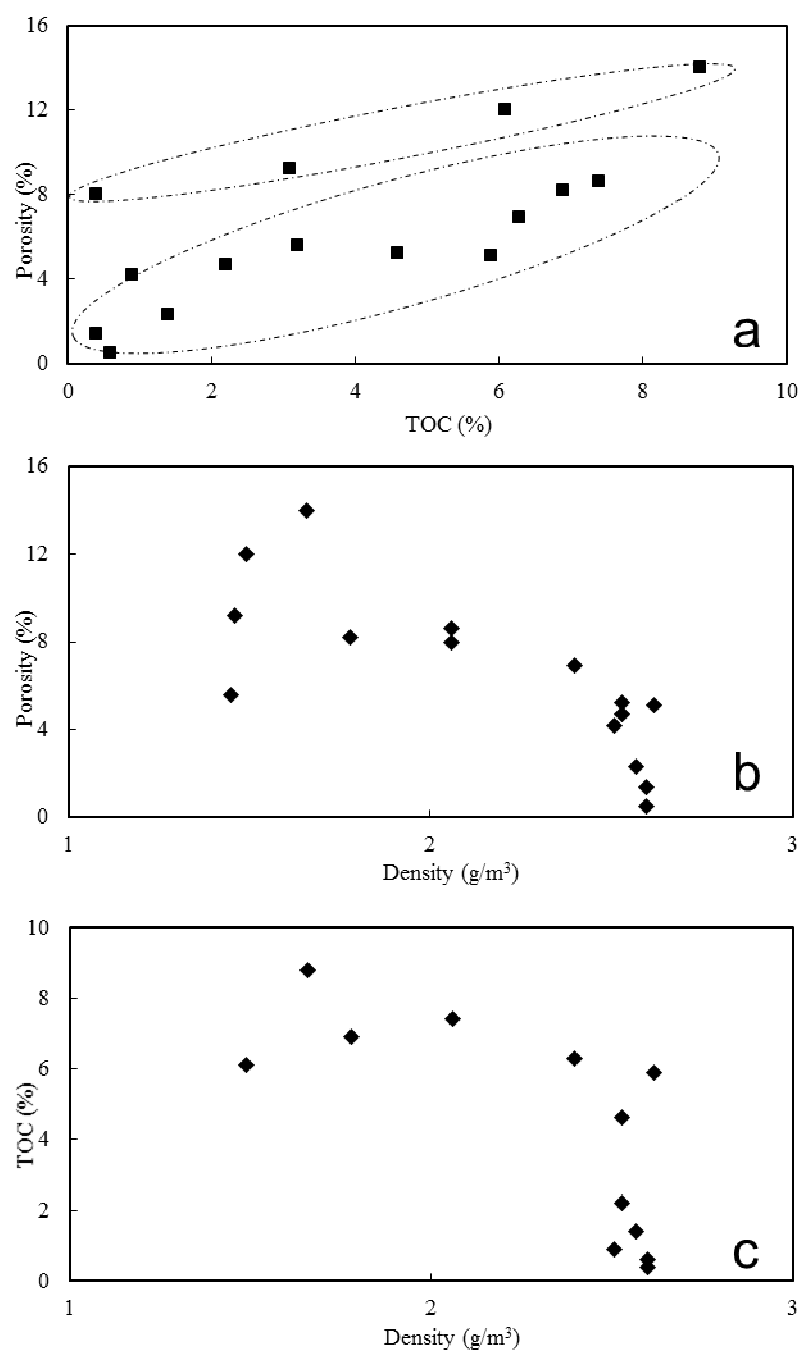Figure 6. Methane adsorption isotherms at 40 °C

Figure 7. Correlation plots of porosity with (a) TOC content, (b) density, and (c) TOC content with density for Permo-Carboniferous shale samples in Central Hunan Province.

- Methane adsorption capacity is between 1.24 cm3/g and 4.53 cm3/g.
- Mean porosity and permeability are 6.4% and 0.013md, respectively.
- Carboniferous and Permian shales are abundant in type III and II organics, respectively.
- Thermal maturity is locating in the wet gas window.
- Mineral constituents are dominated by brittle minerals.